INTERNATIONAL JOURNAL FOR NUMERICAL AND ANALYTICAL METHODS IN GEOMECHANICS
Int. J. Numer. Anal. Meth. Geomech. 2013; **37**:3087–3111
Published online 25 March 2013 in Wiley Online Library (wileyonlinelibrary.com). DOI: 10.1002/nag.2179

Extended finite element framework for fault rupture dynamics including bulk plasticity

Fushen Liu[1] and Ronaldo I. Borja[2,*,†]

[1]*ExxonMobil Research and Engineering, 1545 Route 22 East, Clinton, NJ 08801, U.S.A.*
[2]*Department of Civil and Environmental Engineering, Stanford University, Stanford, CA 94305, U.S.A.*

SUMMARY

We present an explicit extended finite element framework for fault rupture dynamics accommodating bulk plasticity near the fault. The technique is more robust than the standard split-node method because it can accommodate a fault propagating freely through the interior of finite elements. To fully exploit the explicit algorithmic framework, we perform mass lumping on the enriched finite elements that preserve the kinetic energy of the rigid body and enrichment modes. We show that with this technique, the extended FE solution reproduces the standard split-node solution, but with the added advantage that it can also accommodate randomly propagating faults. We use different elastoplastic constitutive models appropriate for geomaterials, including the Mohr–Coulomb, Drucker–Prager, modified Cam-Clay, and a conical plasticity model with a compression cap, to capture off-fault bulk plasticity. More specifically, the cap model adds robustness to the framework because it can accommodate various modes of deformation, including compaction, dilatation, and shearing. Copyright © 2013 John Wiley & Sons, Ltd.

Received 24 August 2012; Revised 27 December 2012; Accepted 2 January 2013

KEY WORDS: extended finite elements; fault rupture dynamics; bulk plasticity

1. INTRODUCTION

Tectonic earthquakes result from spontaneous dynamic rupture and propagation of geologic faults. The energy release from a fault rupture emanates from a combination of frictional heating of the fault surface, bulk plasticity and cracking of the rock near the fault surface, and radiated elastic seismic waves. Closed form solutions for fault rupture dynamics are very difficult if not impossible to obtain, particularly in the presence of bulk plasticity and slip weakening in the host rock. Several numerical methods exist for modeling fault rupture and propagation. The boundary element method (BEM) is a popular choice [1–6], particularly in elastic media. The finite difference method also has been employed [7–11], although it is tricky to use for domains with a complex geometry. Standard explicit finite element (FE) methods have been proposed, along with a so-called 'split-node' formulation combined with a linear slip-weakening law [12–17]. However, they require a priori knowledge of the fault geometry so that the element sides may be aligned to the discontinuity. If the direction of the fault propagation is not known, remeshing will be required by these standard methods, which is undesirable particularly in the presence of bulk plasticity near the fault.

An alternative approach for accommodating a randomly propagating fault is to allow the discontinuity to pass through the interior of the finite elements. To make this feasible, the standard (conforming) FE interpolation must be enriched with a Heaviside function to resolve the propagating discontinuous displacement field. Following this line, formulations based on the assumed enhanced strain

*Correspondence to: Ronaldo I. Borja, Department of Civil and Environmental Engineering, Stanford University, Stanford, CA 94305, U.S.A.
†E-mail: borja@stanford.edu

(AES) [18–29] and extended FE methods [30–38] have been employed. In the AES approach, the enhancements are local to the elements containing the fault, and their contributions are statically condensed on the element level prior to global assembly. The formulation does not engender additional global DOFs, but it results in a discontinuous interpolation of slip across element boundaries. On the other hand, in the extended FE approach, global DOFs are added to the system. This results in a larger system of equations to solve, but the slip is now interpolated continuously across element boundaries. Relevant fault mechanisms including slip weakening and velocity/state-dependent friction have been incorporated successfully into the framework of the AES and extended FE methods [39–43] but only for quasi-static loading. To date, very limited progress has been made to apply either technique to structural dynamics problems.

Liu and Borja [44] and Coon *et al.* [45] were first to use the extended FE approach for simulating fault rupture dynamics. Coon *et al.* proposed a semi-implicit Nitsche's method for updating the tractions on the fault faces. Their method was motivated in large part by numerical stabilization related to the displacement and contact pressure interpolations. However, it is difficult to apply their technique to problems involving bulk plasticity in the neighborhood of the fault. On the other hand, Liu and Borja simulated the fault rupture dynamics with Mohr–Coulomb plasticity and an explicit mass-lumping technique that enhances computational efficiency. They updated the tractions on the fault faces by the penalty method and introduced numerical stabilization through viscous damping. The numerical examples presented by Liu and Borja demonstrate that in the dynamic regime, the traction field on the fault faces does not exhibit spurious oscillation, unlike in the quasi-static case [33]. This is a promising development because it shows the potential of their approach for problems of rupture dynamics and random propagation of geologic faults, as well as for other inherently dynamic problems such as the hydraulic fracturing of rocks [46–49].

This paper builds upon the previous work by Liu and Borja [44] and presents more detailed mathematical formulations and benchmark numerical examples related to the explicit extended FE technique for fault rupture dynamics. The present work compares the performance of different plasticity models for a rock medium hosting a randomly propagating fault, that is, a fault propagating freely through the interior of finite elements. The plasticity models considered in the present work include the Mohr–Coulomb, standard Drucker–Prager, modified Cam-Clay, and capped Drucker–Prager plasticity models, all implemented within the extended FE framework. From the performance of the four aforementioned constitutive models, we find the capped Drucker–Prager model to be most robust inasmuch as it can accommodate inelastic compaction, dilatation, and shearing of rock masses containing a rupturing fault. A final example concerns a spontaneously propagating fault in an elastic medium, in which the propagation direction is calculated as part of the solution. This last example highlights the advantages of the present framework over the split-node technique in that it can accommodate randomly propagating faults.

2. GOVERNING EQUATIONS

Assuming infinitesimal deformation, the balance of linear momentum with inertia load in domain Ω takes the form

$$\nabla \cdot \boldsymbol{\sigma} + \boldsymbol{b} = \rho \ddot{\boldsymbol{u}} \,, \tag{1}$$

where $\boldsymbol{\sigma}$ is the Cauchy stress tensor, $\boldsymbol{b}$ is the body force vector, $\ddot{\boldsymbol{u}}$ is the acceleration vector, ρ is the mass density of the body, and ∇ is the gradient operator. The boundary of Ω is denoted by Γ, which is partitioned into Dirichlet and Neumann boundaries Γ_u and Γ_t, where the displacement and traction are prescribed, respectively. The boundary conditions are as follows:

$$\boldsymbol{u} = \widehat{\boldsymbol{u}} \quad \text{on } \Gamma_u \,, \tag{2}$$

$$\boldsymbol{\sigma} \cdot \boldsymbol{v} = \widehat{\boldsymbol{t}} \quad \text{on } \Gamma_t \,, \tag{3}$$

DOI: 10.1002/nag

where $\boldsymbol{v}$ is the unit normal vector to Γ_t, and $\widehat{\boldsymbol{u}}$ and $\widehat{\boldsymbol{t}}$ are the specified displacement and traction boundary conditions, respectively. We also assume that the initial displacement and velocity of any point $\boldsymbol{x} \in \Omega$ are given as

$$\boldsymbol{u}(\boldsymbol{x}, 0) = \boldsymbol{u}_0(\boldsymbol{x}) \,, \tag{4}$$

$$\dot{\boldsymbol{u}}(\boldsymbol{x}, 0) = \dot{\boldsymbol{u}}_0(\boldsymbol{x}) \,. \tag{5}$$

Let $\mathcal{S}$ denote a fault contained in Ω, with faces $\mathcal{S}_-$ and $\mathcal{S}_+$. Following the formulation presented in [35], the natural boundary conditions on these faces are

$$\boldsymbol{\sigma} \cdot \boldsymbol{n} = \boldsymbol{t}_{\mathcal{S}_-} \quad \text{on } \mathcal{S}_- \,, \tag{6}$$

$$\boldsymbol{\sigma} \cdot (-\boldsymbol{n}) = \boldsymbol{t}_{\mathcal{S}_+} \quad \text{on } \mathcal{S}_+ \,, \tag{7}$$

where $\boldsymbol{n}$ is the unit normal vector to $\mathcal{S}_-$, which is assumed to be in direct contact with $\mathcal{S}_+$. The variational form of dynamic equilibrium may be written as follows. Given $\boldsymbol{b} : \Omega \to \mathbb{R}^{n_{\text{dim}}}$, $\widehat{\boldsymbol{t}} : \Gamma_t \to \mathbb{R}^{n_{\text{dim}}}$, and $\widehat{\boldsymbol{u}} : \Gamma_u \to \mathbb{R}^{n_{\text{dim}}}$, find $\boldsymbol{u} \in \mathcal{U}$ such that for all $\boldsymbol{\eta} \in \mathcal{V}$,

$$\int_\Omega \nabla^{\text{s}} \boldsymbol{\eta} : \boldsymbol{\sigma} \, \mathrm{d}\Omega = \int_\Omega \boldsymbol{\eta} \cdot (\boldsymbol{b} - \rho \ddot{\boldsymbol{u}}) \, \mathrm{d}\Omega + \int_{\Gamma_t} \boldsymbol{\eta} \cdot \widehat{\boldsymbol{t}} \, \mathrm{d}\Gamma \,, \tag{8}$$

where $\boldsymbol{\eta}$ is the first variation of $\boldsymbol{u}$, and ∇^{s} denotes the symmetric component of the gradient operator. The space of trial functions is defined as

$$\mathcal{U} := \left\{ \boldsymbol{u} : \Omega \to \mathbb{R}^{n_{\text{dim}}} \,\middle|\, u_i \in H^1, u_i = \widehat{u}_i \text{ on } \Gamma_{u_i} \right\} \,, \tag{9}$$

whereas the space of variations is defined as

$$\mathcal{V} := \left\{ \boldsymbol{\eta} : \Omega \to \mathbb{R}^{n_{\text{dim}}} | \eta_i \in H^1, \eta_i = 0 \text{ on } \Gamma_{u_i} \right\} \,, \tag{10}$$

where H^1 is the first Sobolev space and n_{dim} is the number of spatial dimensions.

To allow a discontinuous displacement field on the fault, we enrich the displacement field with the Heaviside function $H_{\mathcal{S}}(\boldsymbol{x})$ and write

$$\boldsymbol{u} = \overline{\boldsymbol{u}} + H_{\mathcal{S}}(\boldsymbol{x}) \widetilde{\boldsymbol{u}} \,, \tag{11}$$

where $\overline{\boldsymbol{u}}$ is the continuous part of displacement and $\widetilde{\boldsymbol{u}}$ is the jump in the displacement field. The weighting function is written in a similar form as

$$\boldsymbol{\eta} = \overline{\boldsymbol{\eta}} + H_{\mathcal{S}}(\boldsymbol{x}) \widetilde{\boldsymbol{\eta}} \,. \tag{12}$$

We require that $\overline{\boldsymbol{u}}$, $\widetilde{\boldsymbol{u}}$, $\overline{\boldsymbol{\eta}}$, and $\widetilde{\boldsymbol{\eta}}$ be regular functions (i.e., single valued and analytic). Although these functions are not required to satisfy any specific boundary condition on their own, they must combine so that $\boldsymbol{u} \in \mathcal{U}$ and $\boldsymbol{\eta} \in \mathcal{V}$.

Substituting (11) and (12) into (8) results in two independent variational equations,

$$\int_\Omega \nabla^{\text{s}} \overline{\boldsymbol{\eta}} : \boldsymbol{\sigma} \, \mathrm{d}\Omega = \int_\Omega \overline{\boldsymbol{\eta}} \cdot (\boldsymbol{b} - \rho \ddot{\boldsymbol{u}}) \, \mathrm{d}\Omega + \int_{\Gamma_t} \overline{\boldsymbol{\eta}} \cdot \widehat{\boldsymbol{t}} \, \mathrm{d}\Gamma \tag{13}$$

for the continuous part, and

$$\begin{aligned} \int_\Omega [H_{\mathcal{S}}(\boldsymbol{x}) \nabla^{\text{s}} \widetilde{\boldsymbol{\eta}}] : \boldsymbol{\sigma} \, \mathrm{d}\Omega + \mathcal{G}_{\text{c}}(\widetilde{\boldsymbol{\eta}}, \boldsymbol{t}_{\mathcal{S}_-}) &= \int_\Omega H_{\mathcal{S}}(\boldsymbol{x}) \widetilde{\boldsymbol{\eta}} \cdot (\boldsymbol{b} - \rho \ddot{\boldsymbol{u}}) \, \mathrm{d}\Omega \\ &\quad + \int_{\Gamma_t} H_{\mathcal{S}}(\boldsymbol{x}) \widetilde{\boldsymbol{\eta}} \cdot \widehat{\boldsymbol{t}} \, \mathrm{d}\Gamma \end{aligned} \tag{14}$$

DOI: 10.1002/nag

for the discontinuous part, where $\mathcal{G}_{\mathrm{c}}(\widetilde{\boldsymbol{\eta}}, \boldsymbol{t}_{\mathcal{S}_-})$ is the so-called contact integral representing the contribution from the tractions acting on the fault face $\mathcal{S}_-$. We refer the readers to Liu and Borja [35] for further details relevant to the aforementioned formulations.

3. THE EXTENDED FINITE ELEMENT METHOD

In the extended FE approach, the elements intersected by a discontinuity are enhanced with additional displacement DOFs at the nodes to interpolate the discontinuous displacement field, which is then superimposed to the conforming displacement field. The standard FE approximation for the continuous displacement field $\overline{\boldsymbol{u}}(\boldsymbol{x})$ is given by

$$\overline{\boldsymbol{u}}^h(\boldsymbol{x}) = \boldsymbol{N}(\boldsymbol{x})\boldsymbol{d}\,, \qquad \forall \boldsymbol{x} \in \Omega^h\,, \tag{15}$$

whereas the FE approximation for the discontinuous displacement field $\widetilde{\boldsymbol{u}}(\boldsymbol{x})$ is given by

$$\widetilde{\boldsymbol{u}}^h(\boldsymbol{x}) = \boldsymbol{N}(\boldsymbol{x})H_{\mathcal{S}}(\boldsymbol{x})\boldsymbol{e} = \widetilde{\boldsymbol{N}}(\boldsymbol{x})\boldsymbol{e}\,, \qquad \forall \boldsymbol{x} \in \Omega^h_{\mathcal{S}}\,, \tag{16}$$

where $\Omega^h_{\mathcal{S}}$ is the local support of the surface of discontinuity $\mathcal{S}$, whereas $\boldsymbol{d}$ and $\boldsymbol{e}$ are the nodal displacement vectors interpolating $\overline{\boldsymbol{u}}$ and $\widetilde{\boldsymbol{u}}$, respectively. The matrix form consistent with variational equation (13) is given by

$$\overline{\boldsymbol{M}}\left(\ddot{\boldsymbol{d}}\,, \ddot{\boldsymbol{e}}\right) + \overline{\boldsymbol{F}}_{\mathrm{INT}}(\boldsymbol{d}, \boldsymbol{e}) = \overline{\boldsymbol{F}}_{\mathrm{EXT}}\,, \tag{17}$$

where

$$\overline{\boldsymbol{M}}\left(\ddot{\boldsymbol{d}}\,, \ddot{\boldsymbol{e}}\right) = \left(\int_{\Omega^h} \rho \boldsymbol{N}^{\mathsf{T}}\boldsymbol{N}\,\mathrm{d}\Omega\right)\ddot{\boldsymbol{d}} + \left(\int_{\Omega^h} \rho \boldsymbol{N}^{\mathsf{T}}\widetilde{\boldsymbol{N}}\,\mathrm{d}\Omega\right)\ddot{\boldsymbol{e}}\,, \tag{18}$$

$$\overline{\boldsymbol{F}}_{\mathrm{INT}}(\boldsymbol{d}, \boldsymbol{e}) = \int_{\Omega^h} \boldsymbol{B}^{\mathsf{T}}\boldsymbol{\sigma}(\boldsymbol{d}, \boldsymbol{e})\,\mathrm{d}\Omega\,, \tag{19}$$

and

$$\overline{\boldsymbol{F}}_{\mathrm{EXT}} = \int_{\Omega^h} \boldsymbol{N}^{\mathsf{T}}\boldsymbol{b}\,\mathrm{d}\Omega + \int_{\Gamma^h_t} \boldsymbol{N}^{\mathsf{T}}\boldsymbol{t}\,\mathrm{d}\Gamma\,. \tag{20}$$

We note a slight abuse in the aforementioned notations in that the same symbol $\boldsymbol{\sigma}$ is used for the Cauchy stresses in tensor and vectorized forms. The matrix equation consistent with variational equation (14) is given by

$$\widetilde{\boldsymbol{M}}\left(\ddot{\boldsymbol{d}}, \ddot{\boldsymbol{e}}\right) + \widetilde{\boldsymbol{F}}_{\mathrm{INT}}(\boldsymbol{d}, \boldsymbol{e}) + \mathcal{G}_{\mathrm{c}}(\boldsymbol{e}) = \widetilde{\boldsymbol{F}}_{\mathrm{EXT}}\,, \tag{21}$$

where

$$\widetilde{\boldsymbol{M}}\left(\ddot{\boldsymbol{d}}, \ddot{\boldsymbol{e}}\right) = \left(\int_{\Omega^h_{\mathcal{S}}} \rho \widetilde{\boldsymbol{N}}^{\mathsf{T}}\boldsymbol{N}\,\mathrm{d}\Omega\right)\ddot{\boldsymbol{d}} + \left(\int_{\Omega^h_{\mathcal{S}}} \rho \widetilde{\boldsymbol{N}}^{\mathsf{T}}\widetilde{\boldsymbol{N}}\,\mathrm{d}\Omega\right)\ddot{\boldsymbol{e}}\,, \tag{22}$$

$$\widetilde{\boldsymbol{F}}_{\mathrm{INT}}(\boldsymbol{d}, \boldsymbol{e}) = \int_{\Omega^h_{\mathcal{S}}} \widetilde{\boldsymbol{B}}^{\mathsf{T}}\boldsymbol{\sigma}(\boldsymbol{d}, \boldsymbol{e})\,\mathrm{d}\Omega\,, \tag{23}$$

$$\mathcal{G}_{\mathrm{c}}(\boldsymbol{e}) = \int_{\mathcal{S}} \boldsymbol{N}^{\mathsf{T}}\boldsymbol{t}_{\mathcal{S}_-}\,\mathrm{d}\mathcal{S}\,, \tag{24}$$

DOI: 10.1002/nag

and

$$\widetilde{\boldsymbol{F}}_{\mathrm{EXT}} = \int_{\Omega_S^h} \widetilde{\boldsymbol{N}}^{\mathsf{T}} \boldsymbol{b}\, \mathrm{d}\Omega + \int_{\Gamma_t^h} \widetilde{\boldsymbol{N}}^{\mathsf{T}} \widehat{\boldsymbol{t}}\, \mathrm{d}\Gamma\,. \tag{25}$$

3.1. Explicit time integration

We construct augmented nodal acceleration, velocity, and displacement vectors as

$$\boldsymbol{A} = \begin{Bmatrix} \ddot{\boldsymbol{d}} \\ \ddot{\boldsymbol{e}} \end{Bmatrix}, \qquad \boldsymbol{V} = \begin{Bmatrix} \dot{\boldsymbol{d}} \\ \dot{\boldsymbol{e}} \end{Bmatrix}, \qquad \boldsymbol{D} = \begin{Bmatrix} \boldsymbol{d} \\ \boldsymbol{e} \end{Bmatrix}. \tag{26}$$

The aforementioned vectors contain the standard nodal DOFs $\boldsymbol{d}$, $\dot{\boldsymbol{d}}$, and $\ddot{\boldsymbol{d}}$, plus additional global DOFs $\boldsymbol{e}$, $\dot{\boldsymbol{e}}$, and $\ddot{\boldsymbol{e}}$ at the enriched nodes. We remark that these vectors will normally have variable dimensions as the discontinuity continues to propagate and intersect more finite elements. Next, we combine the FE equations (17) and (21) as follows:

$$\boldsymbol{M}\boldsymbol{A} + \begin{Bmatrix} \overline{\boldsymbol{F}}_{\mathrm{INT}} \\ \widetilde{\boldsymbol{F}}_{\mathrm{INT}} + \boldsymbol{\mathcal{G}}_{\mathrm{c}} \end{Bmatrix} = \begin{Bmatrix} \overline{\boldsymbol{F}}_{\mathrm{EXT}} \\ \widetilde{\boldsymbol{F}}_{\mathrm{EXT}} \end{Bmatrix}, \tag{27}$$

where $\boldsymbol{M}$ is the consistent mass matrix given by

$$\boldsymbol{M} = \begin{bmatrix} \boldsymbol{M}_{11} & \boldsymbol{M}_{12} \\ \boldsymbol{M}_{21} & \boldsymbol{M}_{22} \end{bmatrix}, \tag{28}$$

in which

$$\boldsymbol{M}_{11} = \int_{\Omega^h} \rho \boldsymbol{N}^{\mathsf{T}} \boldsymbol{N}\, \mathrm{d}\Omega\,, \qquad \boldsymbol{M}_{12} = \int_{\Omega_S^h} \rho \boldsymbol{N}^{\mathsf{T}} \widetilde{\boldsymbol{N}}\, \mathrm{d}\Omega\,, \tag{29}$$

$$\boldsymbol{M}_{21} = \boldsymbol{M}_{12}^{\mathsf{T}}, \qquad \boldsymbol{M}_{22} = \int_{\Omega_S^h} \rho \widetilde{\boldsymbol{N}}^{\mathsf{T}} \widetilde{\boldsymbol{N}}\, \mathrm{d}\Omega\,. \tag{30}$$

Given the displacement vector $\boldsymbol{D}_n$ at time t_n, the acceleration vector $\boldsymbol{A}_n$ at the same time instant can be calculated as

$$\boldsymbol{A}_n = \boldsymbol{M}^{-1} \begin{Bmatrix} \overline{\boldsymbol{F}}_{\mathrm{EXT}} \\ \widetilde{\boldsymbol{F}}_{\mathrm{EXT}} \end{Bmatrix}_n - \boldsymbol{M}^{-1} \begin{Bmatrix} \overline{\boldsymbol{F}}_{\mathrm{INT}} \\ \widetilde{\boldsymbol{F}}_{\mathrm{INT}} + \boldsymbol{\mathcal{G}}_{\mathrm{c}} \end{Bmatrix}_n. \tag{31}$$

In an explicit time marching scheme, the augmented velocity and displacement nodal vectors at time t_{n+1} are updated from the formulas

$$\boldsymbol{V}_{n+1/2} = \boldsymbol{V}_{n-1/2} + \Delta t\, \boldsymbol{A}_n\,, \tag{32}$$

$$\boldsymbol{D}_{n+1} = \boldsymbol{D}_n + \Delta t\, \boldsymbol{V}_{n+1/2}\,, \tag{33}$$

where $\Delta t = t_{n+1} - t_n$ is the time increment. Clearly, the only computational burden in the aforementioned algorithm is the inversion of the consistent mass matrix $\boldsymbol{M}$. Mass lumping procedures are typically employed to form a diagonal mass matrix and thus render the simultaneous equation solving trivial.

3.2. Mass lumping technique

Mass lumping is a standard procedure used in structural dynamics along with an explicit time integration scheme [50]. Some computational issues remain unresolved when mass lumping is applied to an element enriched with additional DOFs arising from the extended FE formulation. Specifically, an issue concerns how the total mass of an enriched finite element may be distributed to the nodes to form a diagonal mass matrix. In this paper, we follow the procedure suggested in [51–53] and assume

DOI: 10.1002/nag

that the diagonal terms of the enriched mass matrix have the same value, which is calculated on the basis of the requirement that the kinetic energy of the rigid body and enrichment modes is preserved. The diagonal enriched mass m_L for an arbitrary enrichment function ψ can be written as

$$m_L = \frac{1}{\sum_{i=1}^{\mathrm{NEN}} \psi^2(\boldsymbol{x}_i)} \int_{\Omega_\mathrm{e}} \rho \psi^2 \, \mathrm{d}\Omega_\mathrm{e} \,, \tag{34}$$

where Ω_e is the domain of the enriched element. The Heaviside enrichment function has the property $H_{\mathcal{S}}^2(\boldsymbol{x}) = 1, \ \forall \boldsymbol{x} \in \Omega_\mathrm{e}$, so the enriched lumped mass is simply the total mass divided by the number of element nodes,

$$m_L = \frac{1}{\mathrm{NEN}} \int_{\Omega_\mathrm{e}} \rho \, \mathrm{d}\Omega_\mathrm{e} \,. \tag{35}$$

With the aforementioned mass lumping scheme, we can simply omit the coupled terms in the consistent mass matrix in equation (28), so that both the regular and enriched DOFs can be lumped by the classical row-sum technique.

3.3. Perfectly matched layers

Absorbing boundaries, such as those enriched with dashpots [16], are needed to avoid spurious reflections of waves on the boundaries of an FE mesh. In this paper, we use an explicit perfectly matched layer (PML) on the boundaries to absorb outgoing waves. With the field split method [14, 54] inside the PML region, the equilibrium equation in two dimensions may be written as

$$\begin{aligned} \rho \left(\dot{v}_1^x + d_x v_1^x \right) &= \sigma_{11,1} \,, \\ \rho \left(\dot{v}_2^x + d_x v_2^x \right) &= \sigma_{21,1} \,, \end{aligned} \tag{36}$$

and

$$\begin{aligned} \rho \left(\dot{v}_1^y + d_y v_1^y \right) &= \sigma_{12,2} \,, \\ \rho \left(\dot{v}_2^y + d_y v_2^y \right) &= \sigma_{22,2} \,, \end{aligned} \tag{37}$$

where v denotes a velocity field. The constitutive equation for linear elasticity with damping in the x and y directions may be written as

$$\begin{aligned} \dot{\sigma}_{11}^x + d_x \sigma_{11}^x &= (\lambda + 2\mu) v_{1,1} \,, \\ \dot{\sigma}_{22}^x + d_x \sigma_{22}^x &= \lambda v_{1,1} \,, \\ \dot{\sigma}_{12}^x + d_x \sigma_{12}^x &= \mu v_{2,1} \,, \end{aligned} \tag{38}$$

and

$$\begin{aligned} \dot{\sigma}_{11}^y + d_y \sigma_{11}^y &= \lambda v_{2,2} \,, \\ \dot{\sigma}_{22}^y + d_y \sigma_{22}^y &= (\lambda + 2\mu) v_{2,2} \,, \\ \dot{\sigma}_{12}^y + d_y \sigma_{12}^y &= \mu v_{1,2} \,, \end{aligned} \tag{39}$$

where $\sigma_{ij} = \sigma_{ij}^x + \sigma_{ij}^y$, $v_i = v_i^x + v_i^y$, $i, j = 1, 2$; d_x and d_y are damping profiles in the x and y directions, respectively; and λ and μ are the Lamé constants. At time t_{n-1}, we are given the values

DOI: 10.1002/nag

$\boldsymbol{v}^x_{(n-1/2)}$, $\boldsymbol{v}^y_{(n-1/2)}$, $\boldsymbol{\sigma}^x_{(n-1)}$, and $\boldsymbol{\sigma}^y_{(n-1)}$. Thus, from Equations (38) and (39), the stress components at time t_n may be updated as

$$\begin{aligned}
\sigma^x_{11(n)} &= \left[\Delta t(\lambda+2\mu)v_{1,1(n-1/2)} + (1-\Delta t d_x/2)\sigma^x_{11(n-1)}\right]/(1+\Delta t d_x/2)\,,\\
\sigma^x_{22(n)} &= \left[\Delta t\lambda v_{1,1(n-1/2)} + (1-\Delta t d_x/2)\sigma^x_{22(n-1)}\right]/(1+\Delta t d_x/2)\,,\\
\sigma^x_{12(n)} &= \left[\Delta t\mu v_{2,1(n-1/2)} + (1-\Delta t d_x/2)\sigma^x_{12(n-1)}\right]/(1+\Delta t d_x/2)\,,
\end{aligned} \tag{40}$$

and

$$\begin{aligned}
\sigma^y_{11(n)} &= \left[\Delta t\lambda v_{2,2(n-1/2)} + (1-\Delta t d_y/2)\sigma^y_{11(n-1)}\right]/(1+\Delta t d_y/2)\,,\\
\sigma^y_{22(n)} &= \left[\Delta t(\lambda+2\mu)v_{2,2(n-1/2)} + (1-\Delta t d_y/2)\sigma^y_{22(n-1)}\right]/(1+\Delta t d_y/2)\,,\\
\sigma^y_{12(n)} &= \left[\Delta t\mu v_{1,2(n-1/2)} + (1-\Delta t d_y/2)\sigma^y_{12(n-1)}\right]/(1+\Delta t d_y/2)\,.
\end{aligned} \tag{41}$$

The velocities at time $t_{n+1/2}$ can be updated from the equations

$$\begin{aligned}
\boldsymbol{V}^x_{(n+1/2)} &= \left[-\Delta t\boldsymbol{M}_{\mathrm{L}}^{-1}\boldsymbol{F}^x_{\mathrm{INT}} + (1-\Delta t d_x/2)\boldsymbol{V}^x_{(n-1/2)}\right]/(1+\Delta t d_x/2)\,,\\
\boldsymbol{V}^y_{(n+1/2)} &= \left[-\Delta t\boldsymbol{M}_{\mathrm{L}}^{-1}\boldsymbol{F}^y_{\mathrm{INT}} + (1-\Delta t d_y/2)\boldsymbol{V}^y_{(n-1/2)}\right]/(1+\Delta t d_y/2)\,,
\end{aligned} \tag{42}$$

where $\boldsymbol{M}_{\mathrm{L}}$ denotes the lumped (diagonal) mass matrix, and

$$\boldsymbol{F}^x_{\mathrm{INT}} = \int_\Omega \boldsymbol{B}^{\mathsf{T}}\boldsymbol{\sigma}^x_{(n)}\,\mathrm{d}\Omega\,, \qquad \boldsymbol{F}^y_{\mathrm{INT}} = \int_\Omega \boldsymbol{B}^{\mathsf{T}}\boldsymbol{\sigma}^y_{(n)}\,\mathrm{d}\Omega\,. \tag{43}$$

The damping profile is defined in [14, 54] as

$$d(x) = \frac{3V_{\mathrm{p}}}{2\delta}\log\left(\frac{1}{R}\right)\left(\frac{x}{\delta}\right)^2\,, \tag{44}$$

where V_{p} is the velocity of the compressive wave, δ is the width of the PML, and R is the theoretical reflection coefficient. In the numerical examples, we use $R = 0.00001$, $\delta = 6h$, and h is the element size. Note that the PML formulation described in this section is valid only for linear elasticity problems. To be able to use the PML boundary conditions for elastoplastic problems, we need to ensure that the predicted plastic zones do not reach the PML region. This requires that we have an estimate of the extent of the yield zone so that we can prescribe the PML boundaries to lie outside of that yield zone. The PML idea is similar to the substructure method of Bielak and Christiano [55] for prescribing an effective seismic input for soil–structure interaction analysis: An estimate of the extent of the inelastic region must be made so that it can be contained completely within the substructure.

4. CONSTITUTIVE LAWS

This section describes the relevant constitutive laws governing the elastoplastic response of the host rock inside and outside the fault. Inside the fault, the constitutive response is governed by slip-weakening and friction laws, whereas outside the fault, the response is governed by elasticity and bulk plasticity.

4.1. Slip-weakening friction law

The split-node approach is widely used to model the friction laws on the interface using both the finite difference method [7–9] and the finite element method [12, 15, 16]. The split-node method is also called explicit Lagrange multipliers method (see [56]). We refer the readers to Andrews [8] for the implementation of the split-node approach. This approach does not require additional algorithmic parameters such as a penalty parameter and is suitable for explicit computation with a lumped (diagonal) mass matrix. Unfortunately, applying the approach to the explicit extended FE framework is not

DOI: 10.1002/nag

straightforward because the tractions (i.e., Lagrange multipliers) are typically defined on the integration points along the fault face, but the lumped masses are defined at the nodes. It is not possible to explicitly update the velocity of the nodes directly from the tractions on the fault face, so in this work, we use the penalty method to explicitly update the tractions on the fault face.

We recall that the augmented nodal displacement vector $\boldsymbol{D}_{n+1}$ is determined from equation (33). Assuming no initial penetration between the faces of a fault, the incremental normal gap function is defined as

$$\Delta g_{\mathrm{N},n+1} = \left(\Delta \boldsymbol{u}^{+}_{n+1} - \Delta \boldsymbol{u}^{-}_{n+1}\right) \cdot \boldsymbol{n}\,, \tag{45}$$

where $\Delta \boldsymbol{u}^{+}_{n+1}$ and $\Delta \boldsymbol{u}^{-}_{n+1}$ are the incremental displacements on each side of the fault, and $\boldsymbol{n}$ is the unit normal vector to the fault. The incremental tangential gap function may be calculated as

$$\Delta g_{\mathrm{T},n+1} = \left(\Delta \boldsymbol{u}^{+}_{n+1} - \Delta \boldsymbol{u}^{-}_{n+1}\right) \cdot \boldsymbol{m}\,, \tag{46}$$

where $\boldsymbol{m}$ is the unit tangential vector in the direction of slip. The normal component of the traction vector at time t_{n+1} is updated as

$$t_{\mathrm{N},n+1} = t_{\mathrm{N},n} - \epsilon_{\mathrm{N}} \Delta g_{\mathrm{N},n+1}\,, \tag{47}$$

where ϵ_{N} is a normal penalty parameter that enforces the no-interpenetration requirement approximately. The tangential trial frictional traction at time t_{n+1} is updated as

$$t^{\mathrm{tr}}_{\mathrm{T},n+1} = t_{\mathrm{T},n} - \epsilon_{\mathrm{T}} \Delta g_{\mathrm{T},n+1}\,, \tag{48}$$

where ϵ_{T} is a tangential penalty parameter that forces the tangential slip to approach zero.

The coefficient of friction at time t_{n+1} may be updated from a so-called 'slip-weakening' law. Slip weakening is the process whereby the strength within the fault zone degrades during the initial stage of slip instability. The concept was motivated by the cohesive zone models for tensile fracture developed by Barenblatt [57], Dugdale [58], and Bilby *et al.* [59], and extended to the shear fracture problem by Ida [60] and Palmer and Rice [61]. As the Earth's crust is deformed, the stress increases until it reaches a peak resistance. For intact or relatively undamaged rocks, this peak resistance may consist of frictional and cohesive components along potential faults, whereas for previously faulted rocks, the peak resistance may be predominantly frictional in nature. Once the peak resistance is reached, rocks may fail either by developing a new fault zone or reactivating an old one. The shear strength then decays to a lower level on those segments of the fault that slipped. Various slip-weakening laws have been proposed in the literature; some of which have been calibrated in the laboratory by testing specimens of rocks and inferring the shear fracture energy from these experiments [62–64].

For the present problem, we consider the following slip-weakening law. Let

$$\begin{aligned} &\mu_{n+1} = \mu_d \quad \text{if } g_{\mathrm{T},n+1} > D_c\,, \\ &\mu_{n+1} = \mu_{\mathrm{s}} - \frac{(\mu_{\mathrm{s}} - \mu_d) g_{\mathrm{T},n+1}}{D_{\mathrm{c}}} \quad \text{if } g_{\mathrm{T},n+1} \leqslant D_{\mathrm{c}}\,, \end{aligned} \tag{49}$$

where D_{c} is a characteristic slip over which the coefficient of friction decays from its static to dynamic values. In a way, this parameter is similar to the characteristic slip in the empirical Dieterich–Ruina [65, 66] law for state-dependent and velocity-dependent friction, which has the physical significance of being the slip required to replace a contact population representative of a previous sliding condition with a contact population created under a new sliding condition. If

$$\left|t^{\mathrm{tr}}_{\mathrm{T},n+1}\right| + \mu_{n+1} t_{\mathrm{N},n+1} \leqslant 0\,, \tag{50}$$

then a stick condition holds, and the tangential traction is updated as

$$t_{\mathrm{T},n+1} = t^{\mathrm{tr}}_{\mathrm{T},n+1}\,. \tag{51}$$

DOI: 10.1002/nag

Otherwise, we impose the standard friction law

$$t_{\mathrm{T},n+1} = \mu_{n+1} t_{\mathrm{N},n+1} \left(t^{\mathrm{tr}}_{\mathrm{T},n+1} \Big/ \left| t^{\mathrm{tr}}_{\mathrm{T},n+1} \right| \right) . \tag{52}$$

The terms in the parentheses simply determine the sign of the tangential traction vector from the sign of the predictor value.

4.2. Bulk plasticity

Bulk plasticity pertains to the continuum inelastic deformation of the medium hosting a discontinuity. For rocks, yield criteria must be specified to delimit the extent of the elastic response. In what follows, we present a number of yield criteria along with the corresponding plastic flow rules. We refer the readers to Borja *et al.* [67] for some details pertaining to the plasticity models described in this section.

4.2.1. Mohr–Coulomb criterion. The yield function is given by

$$F = \frac{|\sigma_1 - \sigma_3|}{2} - c\cos\phi + \frac{(\sigma_1 + \sigma_3)}{2}\sin\phi \leqslant 0 . \tag{53}$$

The plastic potential function takes a similar form,

$$G = \frac{|\sigma_1 - \sigma_3|}{2} + \frac{(\sigma_1 + \sigma_3)}{2}\sin\psi . \tag{54}$$

The yield surface for the Mohr–Coulomb model is not smooth but has corners, but for two-dimensional applications, the corners do not activate. The yield surface also has an apex on the tension side of the hydrostatic axis, which does not activate either as long as the mean normal stress remains compressive. The parameters of the model are as follows: ϕ is the friction angle, ψ is the dilation angle, and c is the cohesion; the stress variables are σ_1 and σ_3, the maximum and minimum compressive principal stresses, respectively. We assume perfect plasticity for this yield criterion.

The plastic flow directions are determined by the spectral directions of the elastic stress predictor and the plastic flows in principal axes. The spectral form of the elastic stress predictor is given by

$$\boldsymbol{\sigma}^{\mathrm{tr}} = \sum_{A=1}^{3} \sigma^{\mathrm{tr}}_A \boldsymbol{n}^{(A)} \otimes \boldsymbol{n}^{(A)} , \tag{55}$$

where σ^{tr}_A's are the principal values, and $\boldsymbol{n}^{(A)}$s are the principal directions of $\boldsymbol{\sigma}^{\mathrm{tr}}$ (superscript 'tr' stands for 'trial' or 'predictor'). The incremental plastic strain is then obtained from the flow rule as

$$\Delta\boldsymbol{\epsilon}^{\mathrm{p}} = \Delta\gamma \sum_{A=1}^{3} \frac{\partial G}{\partial \sigma_A} \boldsymbol{n}^{(A)} \otimes \boldsymbol{n}^{(A)} , \tag{56}$$

where G is the plastic potential function;

$$\frac{\partial G}{\partial \sigma_1} = (\zeta_{13} + \sin\psi)/2 , \qquad \frac{\partial G}{\partial \sigma_2} = 0 , \qquad \frac{\partial G}{\partial \sigma_3} = (-\zeta_{13} + \sin\psi)/2 \tag{57}$$

are the plastic flows in principal axes; and $\zeta_{13} = \mathrm{sign}\left(\sigma^{\mathrm{tr}}_1 - \sigma^{\mathrm{tr}}_3\right)$. Note from isotropy that the spectral directions of $\boldsymbol{\sigma}^{\mathrm{tr}}$ and $\Delta\boldsymbol{\epsilon}^{\mathrm{p}}$ coincide.

By using the classical return mapping algorithm, the principal stresses are updated as follows

$$\begin{aligned} \sigma_1 &= \sigma^{\mathrm{tr}}_1 - \Delta\gamma G_1 , \\ \sigma_2 &= \sigma^{\mathrm{tr}}_2 - \Delta\gamma G_2 , \\ \sigma_3 &= \sigma^{\mathrm{tr}}_3 - \Delta\gamma G_3 , \end{aligned} \tag{58}$$

where

$$\begin{aligned} G_1 &= \lambda \sin\psi + \mu(\zeta_{13} + \sin\psi) , \\ G_2 &= \lambda \sin\psi , \\ G_3 &= \lambda \sin\psi + \mu(-\zeta_{13} + \sin\psi) , \end{aligned} \tag{59}$$

DOI: 10.1002/nag

and

$$\Delta\gamma = \frac{2F^{\mathrm{tr}}}{(G_1+G_3)\sin\phi + (G_1-G_3)\zeta_{13}}\,, \\ = \frac{F^{\mathrm{tr}}}{(\lambda+\mu)\sin\psi\sin\phi+\mu}\,. \tag{60}$$

In the aforementioned equations, λ and μ are the Lamé constants, and $F^{\mathrm{tr}} > 0$ is a measure of how much the yield criterion is violated by the predictor stresses.

4.2.2. Drucker–Prager criterion. This is a smooth version of the Mohr–Coulomb plasticity model. The yield function for the Drucker–Prager model is given by

$$F = \sqrt{J_2} + \eta p - \xi c \leqslant 0\,, \tag{61}$$

where

$$J_2 = \frac{1}{2}\boldsymbol{s}:\boldsymbol{s}, \qquad \boldsymbol{s} = \boldsymbol{\sigma} - p\mathbf{1}, \qquad p = \frac{1}{3}\mathrm{tr}(\boldsymbol{\sigma})\,. \tag{62}$$

When the yield surface passes through the outer corners of the Mohr–Coulomb yield surface, we have

$$\eta = \frac{6\sin\phi}{\sqrt{3}(3-\sin\phi)}\,, \qquad \xi = \frac{6\cos\phi}{\sqrt{3}(3-\sin\phi)}\,. \tag{63}$$

The plastic potential function has a similar form, given by

$$G = \sqrt{J_2} + \overline{\eta} p\,, \tag{64}$$

where

$$\overline{\eta} = \frac{6\sin\psi}{\sqrt{3}(3-\sin\psi)}\,. \tag{65}$$

The incremental plastic strain is obtained from the flow rule,

$$\Delta\boldsymbol{\epsilon}^{\mathrm{p}} = \Delta\gamma\frac{\partial G}{\partial\boldsymbol{\sigma}} = \Delta\gamma\left(\frac{\boldsymbol{s}}{2\sqrt{J_2}} + \frac{\overline{\eta}}{3}\mathbf{1}\right)\,, \tag{66}$$

where $\mathbf{1}$ is the second-order identity tensor. The deviatoric and volumetric stresses are updated from classical return mapping through the equations

$$\boldsymbol{s} = \left(1 - \frac{\mu\Delta\gamma}{\sqrt{J_2^{\mathrm{tr}}}}\right)\boldsymbol{s}^{\mathrm{tr}}\,, \tag{67}$$

and

$$p = p^{\mathrm{tr}} - \Delta\gamma K\overline{\eta}\,, \tag{68}$$

where K and μ are the elastic bulk and shear moduli, respectively. The incremental plastic strain is obtained from the consistency condition

$$\Delta\gamma = F^{\mathrm{tr}}/\left(\mu + K\eta\overline{\eta}\right)\,. \tag{69}$$

We also assume perfect plasticity for this model.

DOI: 10.1002/nag

4.2.3. Modified Cam-Clay model. The yield function has the shape of an ellipse on the p-q plane,

$$F = \frac{1}{b^2}(p - p_t + a)^2 + \frac{1}{M^2}q^2 - a^2 \leqslant 0\,, \tag{70}$$

where the parameter b is defined by

$$b = \begin{cases} 1 & \text{if } p \geqslant p_t - a \\ \beta & \text{if } p < p_t - a \end{cases}. \tag{71}$$

The parameter a defines the radius of the right half of an ellipse, β is a material constant, and βa defines the modified radius of the left half of the ellipse on the compressive side of the hydrostatic axis. We also have

$$p_t = c\xi/\eta \tag{72}$$

and

$$M = \sqrt{3/2}\eta\,, \qquad q = \sqrt{3J_2/2}\,. \tag{73}$$

The hardening variable is defined in terms of the absolute value of the cumulative volumetric plastic strain,

$$\alpha = -\int_0^t \dot{\epsilon}_v^{\mathrm{p}}\,\mathrm{d}t\,. \tag{74}$$

The radius a of the ellipse varies according to a linear hardening law

$$a = a_0 + H\alpha\,, \tag{75}$$

where a_0 is the initial radius of the ellipse and H is the plastic modulus. To calculate the plastic strains, we assume an associative flow rule and evaluate the incremental plastic strains from

$$\Delta\boldsymbol{\epsilon}^{\mathrm{p}} = \Delta\gamma\frac{\partial F}{\partial\boldsymbol{\sigma}} = \Delta\gamma\left[\frac{3}{M^2}\boldsymbol{s} + \frac{2}{b^2}(p - p_t + a)\mathbf{1}\right]. \tag{76}$$

The stress variables p and q are updated from classical return mapping,

$$p = p^{\mathrm{tr}} + K(\alpha - \alpha_n) \tag{77}$$

and

$$q = \frac{M^2}{M^2 + 6\mu\Delta\gamma}q^{\mathrm{tr}}\,. \tag{78}$$

We use Newton's method to solve for α and $\Delta\gamma$ simultaneously from the hardening law

$$\alpha - \alpha_n + \Delta\gamma\frac{2}{b^2}[p(\alpha) - p_t + a(\alpha)] = 0\,, \tag{79}$$

and the consistency condition

$$\frac{1}{b^2}[p(\alpha) - p_t + a(\alpha)]^2 + \frac{1}{M^2}q(\Delta\gamma)^2 - a(\alpha)^2 = 0\,. \tag{80}$$

DOI: 10.1002/nag

4.2.4. Capped Drucker–Prager model. The yield function is a combination of the standard Drucker–Prager model and modified Cam-Clay model representing the dilation and compression sides, respectively, that is,

$$F_1 = \sqrt{J_2} + \eta p - \xi c \leqslant 0 \tag{81}$$

for the dilation side, and

$$F_2 = \frac{1}{b^2}[p - p_t + a]^2 + \frac{1}{M^2}q^2 - a^2 \leqslant 0 \tag{82}$$

for the compression side. Once again, we use a nonassociative Drucker–Prager formulation for the dilatant response,

$$G_1 = \sqrt{J_2} + \overline{\eta} p\,, \tag{83}$$

and an associative flow rule for the compressive response. The return mapping algorithm is similar to the previous subsections, with the exception that a special treatment is employed on the corner where the two yield functions meet in a nonsmooth fashion. We use Koiter's rule and write the incremental plastic strain as

$$\Delta\boldsymbol{\epsilon}^{\mathrm{p}} = \Delta\gamma_1 \left(\frac{\boldsymbol{s}}{2\sqrt{J_2}} + \frac{\overline{\eta}}{3}\mathbf{1} \right) + \Delta\gamma_2 \frac{3}{M^2}\boldsymbol{s}\,, \tag{84}$$

where $\Delta\gamma_1$ and $\Delta\gamma_2$ are two consistency conditions satisfying both yield criteria on the corner. In general, they may be solved iteratively using Newton's method.

4.3. Viscous damping

It is necessary to introduce viscous damping to stabilize the traction field on the fault. With the stiffness damping approach, we use the effective stress $\widetilde{\boldsymbol{\sigma}}$ (similar to a Kelvin–Voigt model) to calculate the internal nodal force vector $\boldsymbol{F}_{\mathrm{INT}}$,

$$\widetilde{\boldsymbol{\sigma}} = \boldsymbol{\sigma} + \xi \boldsymbol{C}^{\mathrm{e}} : \dot{\boldsymbol{\epsilon}}\,, \tag{85}$$

where ξ is a damping coefficient, $\boldsymbol{C}^{\mathrm{e}}$ is the elasticity tensor, and $\dot{\boldsymbol{\epsilon}}$ is the strain rate. The Cauchy stress tensor $\boldsymbol{\sigma}$ is calculated from the elastoplastic constitutive laws.

A detailed motivation for the stiffness damping parameter ξ is suggested in [12]: $\xi = \beta\alpha h / V_{\mathrm{p}}$, where h is the mesh size, V_{p} is the velocity of the compressive wave, α is the CFL number, with typical values $0.0 < \alpha < 1.0$, and β is a nondimensional parameter used to adjust the damping parameter, with typical values $0.0 < \beta < 1.0$. On the basis of these numbers, we select a stiffness damping parameter $\xi = 0.001$ for the elastic problems described in the next section. Viscous damping is not as critical for elastoplastic problems, because another type of damping, hysteretic damping due to inelastic deformation, may also be present [68, 69]. Nevertheless, we still use a much smaller damping, $\xi = 0.000014$, to suppress high-frequency noise.

5. NUMERICAL EXAMPLES

We consider four examples in this section in which the fault geometry is fully specified. A fifth example deals with the creation of a new fault whose geometry evolves with the solution and cannot be specified a priori. This last example highlights the advantage of the proposed formulation in that it can deal with problems where the fault geometry is not initially specified.

5.1. Lamb's problem

We use Lamb's problem [70] as our first numerical example to test the penalty method for the case of a 'glued' interface. This example also serves to test the PML implementation for the absorbing boundary within the context of the proposed explicit extended FE framework for spontaneous dynamic rupture. The same problem was also solved in [15]. The problem involves a Gaussian-type point force

DOI: 10.1002/nag

$f(t) = \exp[-1000(t-t_0)^2]$ applied to the surface of a half space, herein modeled with a mesh of constant strain triangular (CST) elements, where the delay time $t_0 = 0.25$ s, density $\rho = 2700$ kg/m^3, compressive wave velocity $V_p = 6000$ m/s, and shear wave velocity $V_s = 3464$ m/s are assumed. The computational domain has dimensions of 2×20 km. The half-space is discretized into uniform right-angle CST elements with a side length of $h = 10$ m, resulting in the creation of 40,2201 nodes and 800,000 CST elements. We use the PML for all the boundaries except at the top free surface, and the width of the PML is taken as $\delta = 6h$. An analytical solution is available for this problem based on the Cagniard–de Hoop technique [71]. The time step for the regular CST elements is taken as $\Delta t = 0.0005$ s. No viscous damping is used in the interior domain.

For the extended FE method with a horizontal glued fault inside, we prescribe penalty parameter values of $\epsilon_N = \epsilon_T = 10^9$ MN/m and a time step of $\Delta t = 0.0001$ s. We set the cohesion of the fault

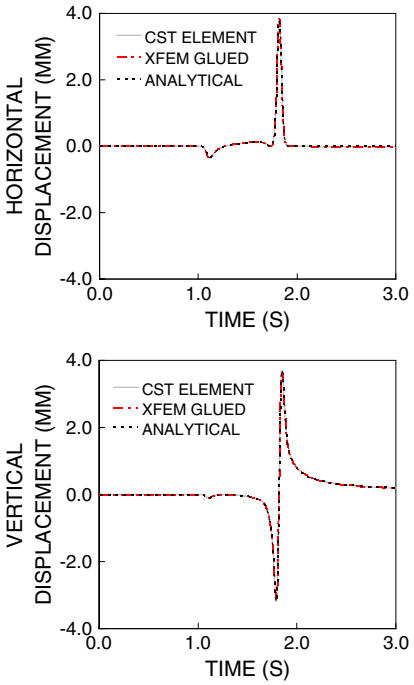

Figure 1. Comparison of the finite element and analytical solutions for Lamb's problem: The observation point on the surface is at 5 km from the source. No filtering is used in plotting the aforementioned figures. Note that the plots are approximately one on top of the other. CST, constant strain triangular; XFEM, extended finite element method.

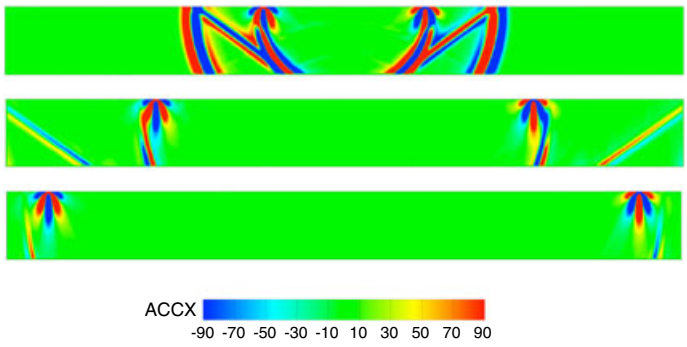

Figure 2. Contours of particle horizontal accelerations (ACCX) at time $t = 1.0$ (top), 2.0 (middle), and 3.0 s (bottom). Color bar in mm/s^2.

DOI: 10.1002/nag

surface to a very large number to prevent the surface from slipping. The numerical and analytical displacement time histories at the receiver point, located on the free surface 5 km from the source point, are shown in Figure 1. Unlike the simulations reported in [15], no viscous damping was used in the present computation, and no low-pass filtering technique for postprocessing was used for plotting Figure 1. The contours of horizontal and vertical accelerations at different time instants (1.0, 2.0, and 3.0 s) are shown in Figures 2 and 3. We see that the extended FE formulation reproduces the results of the standard split-node solution utilizing regular CST elements. Figures 2 and 3 also show no significant wave reflections generated by the PML.

5.2. *Elastic dynamic rupture problem*

To test the performance of the proposed framework for dynamic rupture simulations, we consider the dynamic rupture problem TPV205-2D from the Southern California Earthquake Center/United States Geological Survey (SCEC/USGS) Earthquake Code Verification Exercise. The dimensions of the computational domain are 60×40 km^2. The center of a horizontal fault is located at the center of the mesh, that is, at coordinates (30 km, 20 km), and the length of the fault is $L = 50$ km, with end points at $x = 5$ km and $x = 55$ km. The domain is assumed to be homogeneous and linearly elastic, with compressive wave velocity $V_p = 6.0$ km/s, shear wave velocity $V_s = 3.464$ km/s, and density $\rho = 2670$ kg/m^3. The fault can only rupture in the region L_r, defined by the range $15.0 \text{ km} \leqslant x \leqslant 45.0$ km; outside this region, the fault is forced to remain in stick mode by assigning a very high static coefficient of friction on the appropriate fault segments to prevent them from slipping.

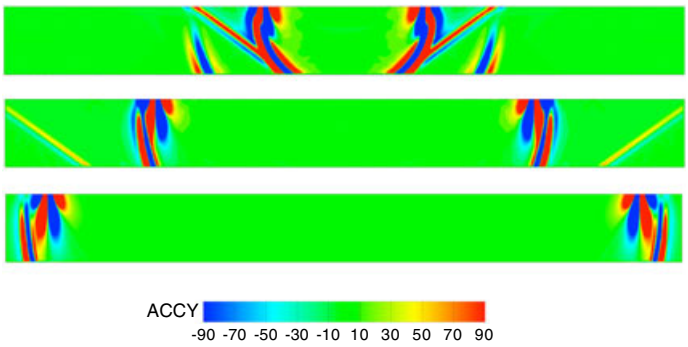

Figure 3. Contours of particle vertical accelerations (ACCY) at time $t = 1.0$ (top), 2.0 (middle), and 3.0 s (bottom). Color bar in mm/s^2.

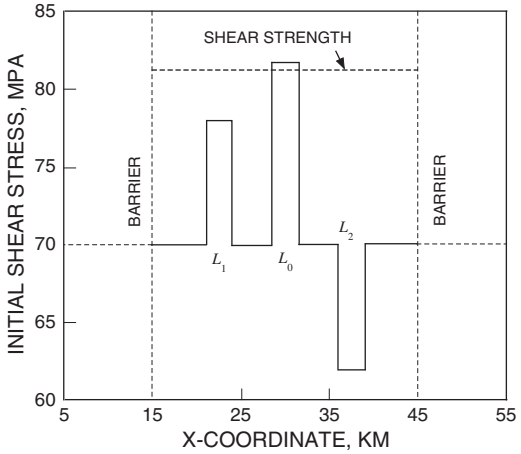

Figure 4. Initial shear stress distribution on the fault surface. 'Barrier' denotes the extent of the stick mode.

DOI: 10.1002/nag

Inside the region L_r, the static coefficient of friction is assumed to have a value $\mu_s = 0.677$, whereas the dynamic coefficient of friction is assumed to have a value $\mu_d = 0.525$. The slip-weakening critical distance is taken as $D_c = 0.4$ m.

We subject the fault to initial normal stress of $t_N = 120$ MPa and initial shear stress of $t_T = 70$ MPa; however, we also introduce several initial shear stress states into the fault surface to generate unsymmetric and inhomogeneous conditions. This is realized by defining three-fault regions, $L_0 : \{28.5 \leqslant x \leqslant 31.5\}$, $L_1 : \{21.0 \leqslant x \leqslant 24.0\}$, and $L_2 : \{36.0 \leqslant x \leqslant 39\}$ (all in km). In region L_1, the initial shear stress is assumed to be $t_T^1 = 78$ MPa, and in region L_2, the initial shear stress is set to $t_T^2 = 62$ MPa. In the region L_0, the initial shear stress is set to $t_T^0 = 81.6$ MPa, which is greater than the static shear strength of the fault, $t_T^c = 81.24$ MPa. Consequently, L_0 defines the fault segment that would be first to rupture. Figure 4 summarizes the initial shear stresses.

For the simulation, we consider element sizes $h = 100$ m and $h = 50$ m, penalty parameters $\epsilon_N = \epsilon_T = 1.0 \times 10^7$, time step $\Delta t = 0.001$ s, and simulation duration $t = 12$ s. To stabilize the problem, we introduce a slight viscous damping into the system, $\xi = 0.001$ (see Section 4.3). Figure 5

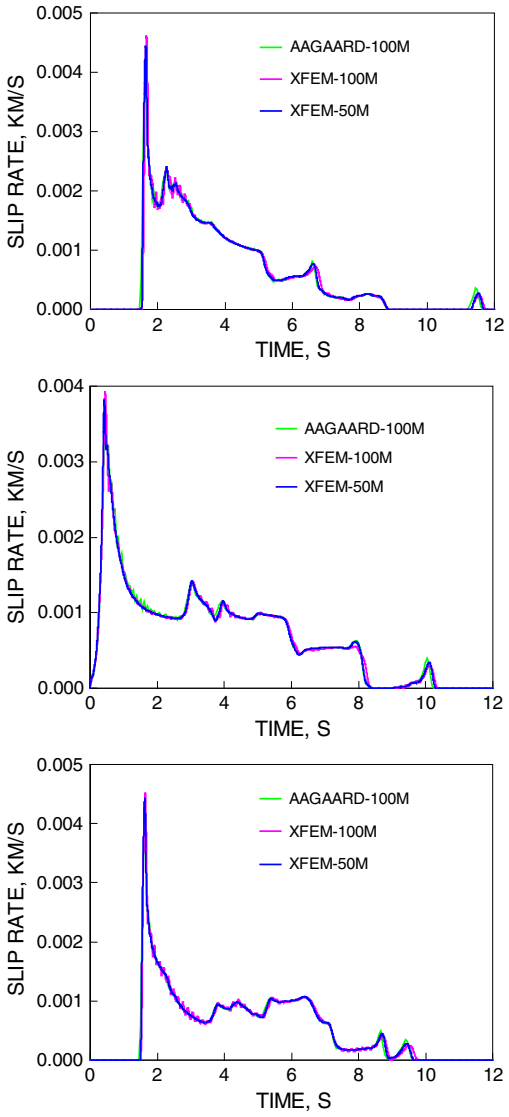

Figure 5. Comparison of slip rate versus time histories at $x = 25.5$ km (top), $x = 30$ km (middle), and $x = 34.5$ km (bottom). Note that the plots are approximately one on top of the other. XFEM, extended finite element method.

DOI: 10.1002/nag

shows the fault slip rate time histories at $x = 25.5$ km, $x = 30$ km, and $x = 34.5$ km. For verification purposes, the figure compares our results with those obtained by Brad Aagaard [72] from the SCEC/USGS Earthquake Code Verification Exercise. Aagaard used the split-node approach with an element dimension of 100 m in his numerical simulations. In general, our calculated slip rates match Aagaard's results very well. Figure 6 shows the on-fault shear stress time history, at $x = 25.5$ km, $x = 30$ km, and $x = 34.5$ km. We observe a noticeable error for the 100-m shear stress compared with Aagaard's results because we used the penalty methods to update the shear stress. However, the error goes away when we refined the mesh to $h = 50$ m. To test the influence of the penalty parameter on the calculated results, we changed the penalty parameters to $\epsilon_{\mathrm{N}} = \epsilon_{\mathrm{T}} = 5.0\times10^{7}$ and $\epsilon_N = \epsilon_T = 5.0\times10^{6}$ for the 50-m discretization. Compared with the corresponding results with $\epsilon_{\mathrm{N}} = \epsilon_{\mathrm{T}} = 1.0 \times 10^{7}$, Figure 7 shows that the penalty parameters do not significantly influence the calculated slip rate/time histories.

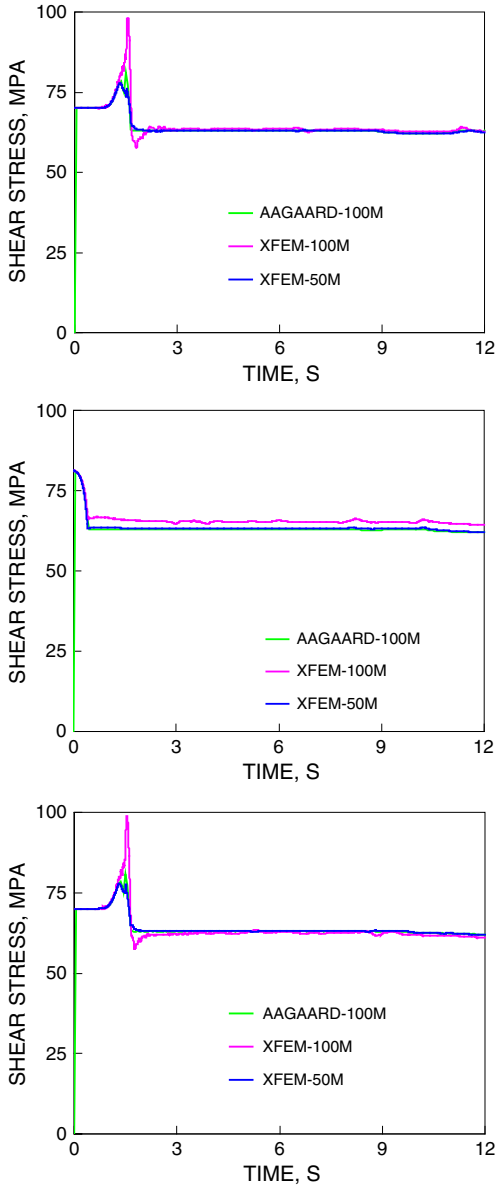

Figure 6. Comparisons of shear stress versus time histories at $x = 25.5$ km (top), $x = 30$ km (middle), and $x = 34.5$ km (bottom). XFEM, extended finite element method.

DOI: 10.1002/nag

5.3. *Elastoplastic dynamic rupture problem*

We revisit Andrews' model [9] describing dynamic rupture with bulk (off-fault) plasticity, along with the Mohr–Coulomb yield criterion. The bulk material is assumed to be uniform and isotropic, with density $\rho = 2700$ kg/m^3, compressive wave velocity $V_p = 5.196$ km/s, and shear wave velocity $V_s = 3.0$ km/s. The initial stress state is assumed to be uniform with $\sigma_{11} = \sigma_{22} = -50$ MPa and $\sigma_{12} = 10$ MPa. The coefficient of static friction is set to 0.5, whereas the coefficient of kinetic friction is assumed to be zero. We also assume the following parameters for the Mohr–Coulomb model: cohesion $c = 0$, friction angle $\phi = 37°$, and dilation angle $\psi = 0$ (isochoric plastic flow). Andrews used a time-weakening law where the coefficient of friction decreases to the kinetic value over a characteristic time interval $T_c = 0.0035$ s after the shear traction on the fault reaches the static frictional strength. With the aforementioned time-dependent relaxation law, the adjusted plastic flow parameter becomes

$$\Delta\gamma_i \leftarrow \Delta\gamma_i (1 - \exp(-\Delta t / T_v)) , \tag{86}$$

where $T_v = 0.00067$ s is the critical relaxation time. The aforementioned equation simply implies that plastic strains at each time step are scaled by the time relaxation to enable us to compare our results with [9] and thus verify our implementation. A small stiffness damping coefficient $\xi = 0.000014$ is used in the simulations (see Section 4.3), and the penalty parameters are set to $\epsilon_N = \epsilon_T = 5.0 \times 10^7$. The contours of plastic strain at time $t = 0.785$ s are shown in Figure 8 for a computational domain of 0.5×8.0 km, assuming the fault nucleated at point (4.0,0.25) km over a nucleation length of $L_c = 60$ m, with an element size $h = 0.002$ km. In general, the off-fault plastic strains are very close to the

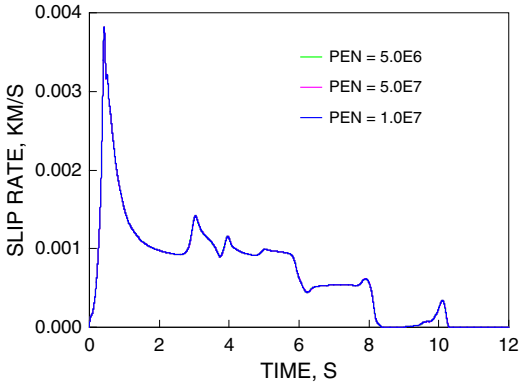

Figure 7. Variation of slip rate with time at $x = 30$ km showing lack of sensitivity of the slip rate to values of the penalty parameters (PEN). Note that the plots are approximately one on top of the other.

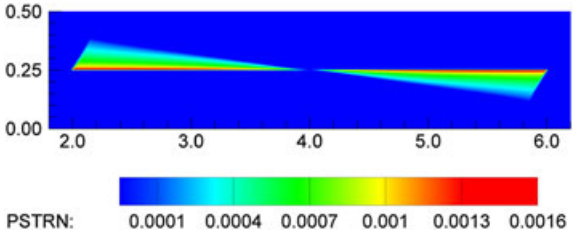

Figure 8. Off-fault plastic strains (PSTRN) at time $t = 0.785$ s: The maximum value of plastic strain is 0.0016 along the fault, which agrees with the calculated value obtained by Andrews [9].

DOI: 10.1002/nag

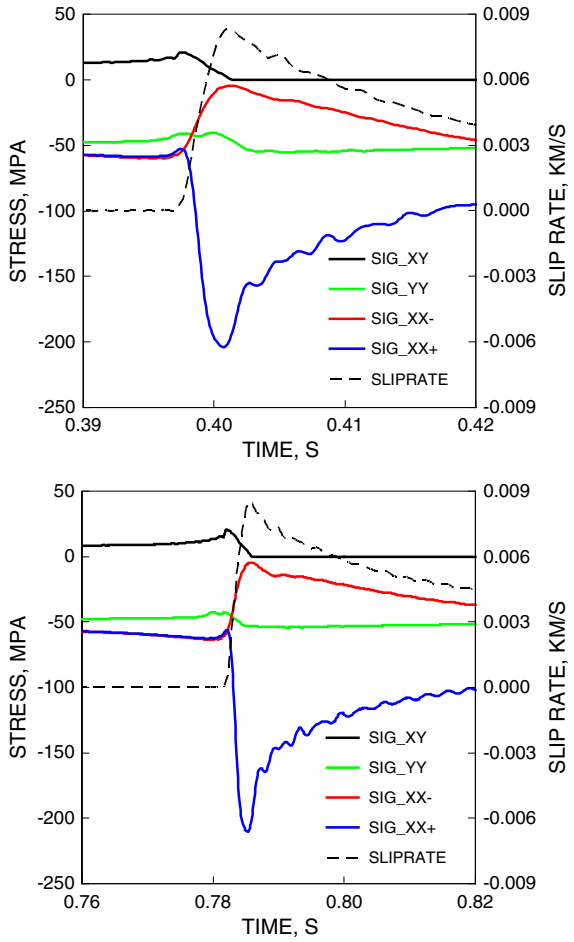

Figure 9. On-fault slip rate and stress components time history at $x = 5.0$ km (top) and $x = 6.0$ km (bottom).

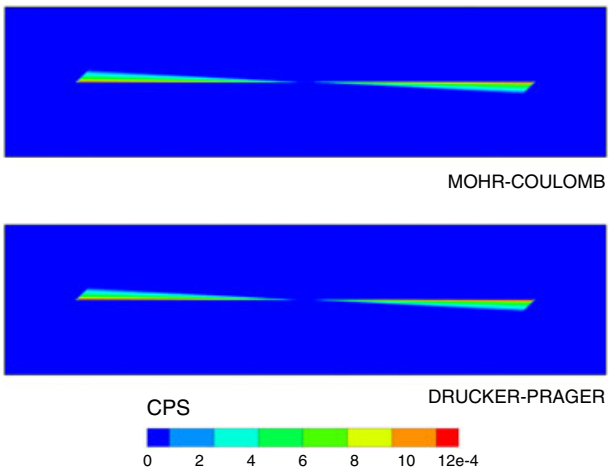

Figure 10. Off-fault plastic strains at time $t = 0.6$ s calculated with the Mohr–Coulomb and Drucker–Prager plasticity models. CPS, cumulative plastic strain.

ones obtained by Andrews. The time histories of slip rate and stress component at $x = 5.0$ km and $x = 6.0$ km are shown in Figure 9.

DOI: 10.1002/nag

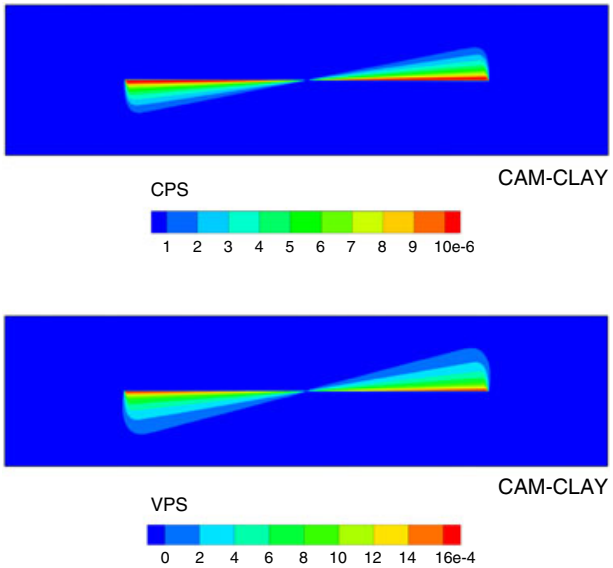

Figure 11. Off-fault plastic strains at time $t = 0.6$ s calculated with the modified Cam-Clay model. CPS, cumulative plastic strain; VPS, volumetric plastic strain.

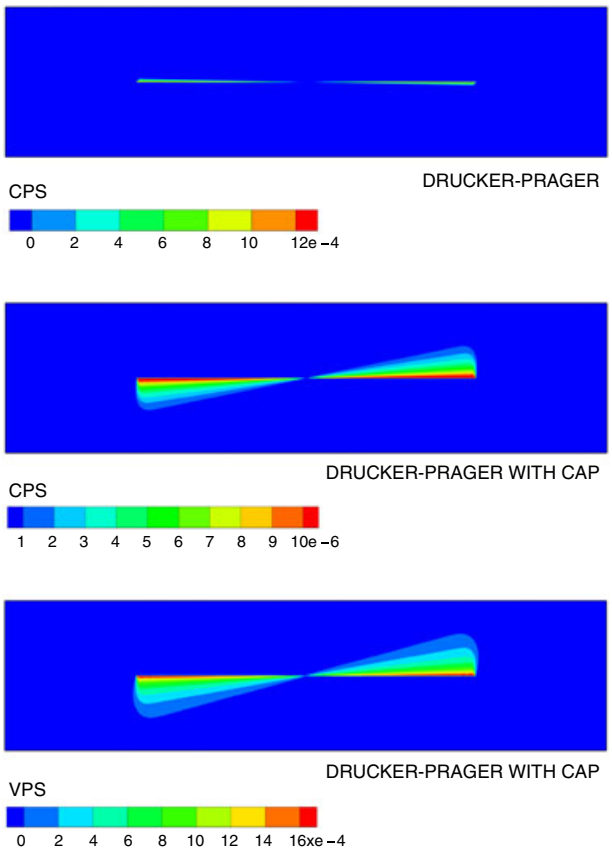

Figure 12. Off-fault plastic strains at time $t = 0.6$ s calculated with the capped Drucker-Prager plasticity model. CPS = cumulative plastic strain; VPS = volumetric plastic strain; CAP, compression cap.

DOI: 10.1002/nag

5.4. *Comparison of different plasticity models*

In this example, we compare the fault rupture dynamics calculated by the extended FE code using four classical plasticity models for geomaterials: Mohr–Coulomb, Drucker–Prager, modified Cam-Clay, and Drucker–Prager with a compression cap. For the bulk material, we assume frictional angle $\phi = 36.87°$, dilatancy angle $\psi = 15°$, cohesion $c = 5.0$ MPa, initial radius of the ellipse $a = 40$ MPa, radius ratio $\beta = 0.5$, and hardening parameter for the ellipse $H = 0.1$. The computational domain is 1.0×4.0 km. All other parameters are the same as in the previous example except that no time relaxation was used for the plastic strains. Figure 10 shows the plastic zones predicted by the Mohr–Coulomb and Drucker–Prager models, and Figures 11 and 12 the plastic zones predicted by the modified Cam-Clay and compression cap models, respectively. Note that the modified Cam-Clay and

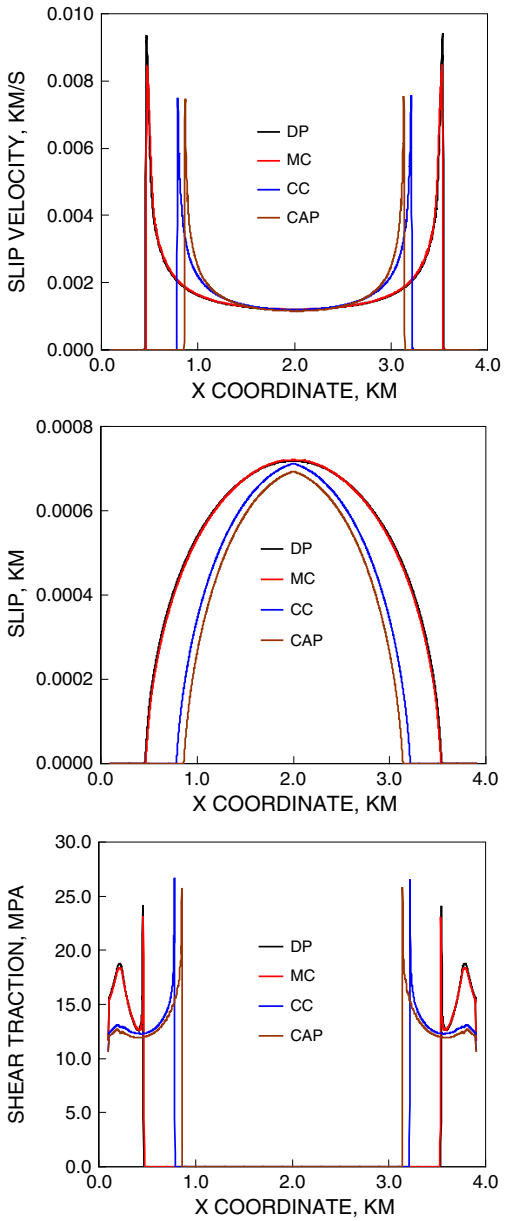

Figure 13. Comparison of slip velocities, slips, and shear tractions at time $t = 0.6$ s computed with the four plasticity models. DP, Drucker–Prager; MC, Mohr–Coulomb; CC, modified Cam-Clay; CAP, compression cap.

DOI: 10.1002/nag

compression cap models predict larger plastic zones in the compression region. Figure 13 compares the slip velocity, slip, and shear traction distributions predicted by the four different bulk constitutive models. As expected, the Mohr–Coulomb and Drucker–Prager models predict similar plastic zones, as well as similar slip and shear traction distributions. The modified Cam-Clay and compression cap models predict smaller rupture velocities, narrower slip regions, and smaller magnitudes of slip on the fault. This is because a portion of the energy released during rupture is dissipated into volumetric plastic compaction, and so, the fault tips did not propagate as far as they would advance if the yield surfaces did not have a compression cap.

5.5. *Dynamic fault propagation*

In this example, we explore the capability of the extended FE framework to study fault growth in an elastic medium where the direction of fault propagation is not a priori known. The material parameters are the same as in Section 5.2. The dimensions of the computational domain are 60×20 km, with the lower left-hand corner of the domain located at the origin of a Cartesian reference frame. An initial horizontal fault 8 km long was centered in the domain at coordinates (30 km, 10 km). Fault rupture was triggered by reducing the frictional coefficient to a dynamic value over a nucleation length defined by the range $L_n := \{x | 28.5 \text{ km} \leqslant x \leqslant 31.5 \text{ km}\}$. The initial stresses inside the computational domain are set to $\sigma_{11} = \sigma_{22} = -120$ MPa and $\sigma_{12} = 70$ MPa.

To predict the growth path of a newly generated fault, certain fracture and propagation criteria must be prescribed. In this example, we used the Coulomb criterion for failure in shear (see the textbook by Pollard and Fletcher [73], pp. 357–364). The angle γ_c between the critical slip plane and the direction of the maximum compressive stress is given as

$$\gamma_c = \frac{1}{2} \arctan\left(\frac{1}{\mu_s}\right), \tag{87}$$

where μ_s is the static frictional coefficient of the fault surface. The Coulomb stress is defined as

$$\sigma_{CC} = \frac{1}{2}(\sigma_1 - \sigma_3)\left(1 + \mu_s^2\right)^{1/2} + \frac{1}{2}(\sigma_1 + \sigma_3)\mu_s, \tag{88}$$

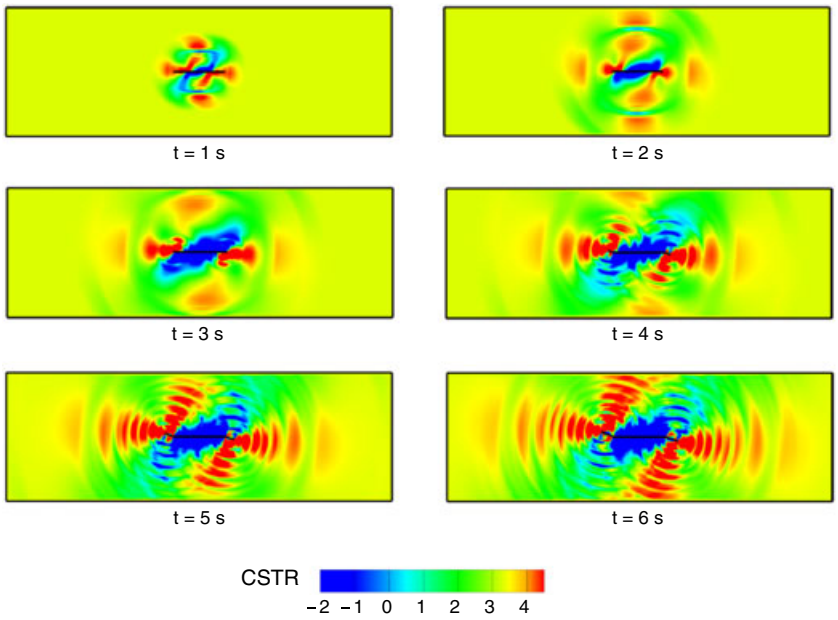

Figure 14. Fault rupture dynamics and random propagation of new fault faces. CSTR, Coulomb stress in MPa.

DOI: 10.1002/nag

where σ_1 and σ_3 are the maximum and minimum principal stresses, respectively (i.e., minimum and maximum compressive stresses, respectively). If the Coulomb stress σ_{CC} is greater than an inherent shear cohesion c_0, new slip planes are generated. In general, the Coulomb criterion predicts two sets of slip planes with an equal likelihood of mobilization. For purposes of analysis, we selected the slip plane that is closer to the horizontal plane, because the initial fault is defined by a horizontal plane. The shear cohesion is assumed to be $c_0 = 3.5$ MPa. Every 0.5 s, we evaluate the Coulomb stresses for each fault tip and propagate the fault once the Coulomb fracture criterion is reached. We prescribe a propagation length of $\Delta L = 0.30$ km for newly generated fault segments and set the initial traction on newly generated fault faces to be equal to the bulk stress projected on the fault face.

Figures 14 and 15 show the predicted fault nucleation and random propagation processes considering both the shear rupture propagation along the given initial fault and the random generation of new fault faces. The calculated Coulomb stresses are also shown as they radiate away from the nucleating fault segments. Because of the uniform initial stress distribution assumed in the simulation, the stress

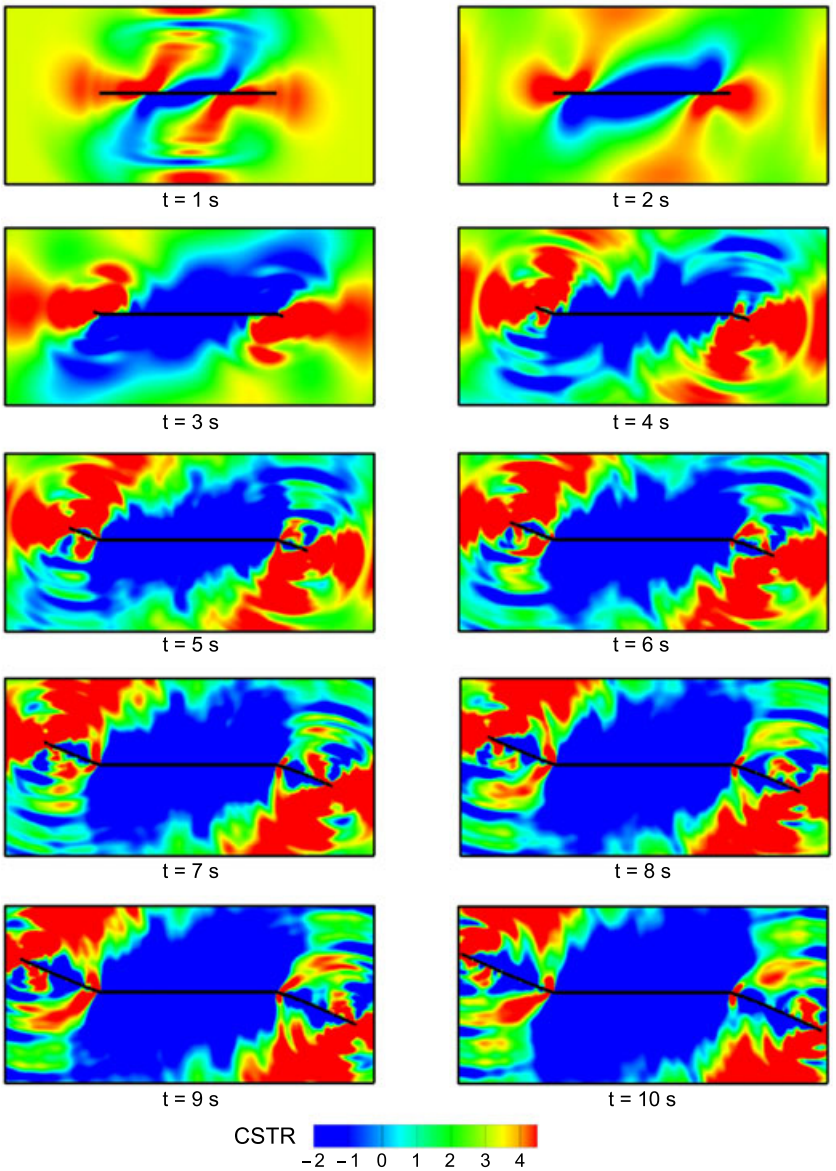

Figure 15. Zoom on fault rupture dynamics and random propagation of new fault faces. Color bar is Coulomb stress (CSTR) in MPa.

DOI: 10.1002/nag

waves show an antisymmetric pattern where depth effects are not present. More realistic simulations may involve the effect of nonuniform stress distribution accounting for depth effects, which would make the stress wave pattern less antisymmetric. We remark that it would be difficult to use the classical split-node technique for this problem because it cannot readily accommodate the creation of new fault faces and the random advance of fault tips.

6. SUMMARY AND CONCLUSIONS

We have presented a fully explicit extended FE framework for simulating fault rupture dynamics in elastoplastic media. The method is more robust than the traditional split-node technique in that it can accommodate randomly propagating faults whose geometry may not be known a priori but instead may have to be calculated as part of the solution. We verified the numerical framework by comparing the dynamic responses with analytical and numerical solutions for some complex BVPs reported in the literature. More specifically, the extended FE framework reproduces the split-node solutions for some of these complex BVPs. An advantage of the proposed solution is that it can accommodate the creation of new fault faces whose inclinations may depend on the evolving stress configuration. We also have demonstrated the capability of the framework to accommodate bulk plasticity in the vicinity of the fault. From among the four elastoplastic constitutive models presented in this paper, we find the Drucker–Prager plasticity model with a compression cap to be most versatile in that it encapsulates different modes of inelastic deformation relevant to fault rupture processes, including compaction, dilatation, and shearing.

ACKNOWLEDGEMENTS

We thank the two reviewers for their detailed reviews and for the numerous constructive suggestions to improve the presentation aspects of the paper. The first author acknowledges a Stanford Graduate Fellowship (SGF) that partially supported this research conducted between years 2008 and 2010. He also thanks ExxonMobil management for approving the release of this work. The second author acknowledges support from the US Department of Energy under grant no. DE-FG02-03ER15454 to Stanford University.

REFERENCES

1. Andrews DJ. Dynamic plane-strain shear rupture with a slip-weakening friction law calculated by a boundary integral method. *Bulletin of the Seismological Society of America* 1985; **75**:1–21.
2. Ben-Zion Y, Rice JR. Dynamic simulations of slip on a smooth fault in an elastic solid. *Journal of Geophysical Research* 1997; **102**:17771–17784.
3. Cochard A, Madariaga R. Dynamic faulting under rate-dependent friction. *Pure and Applied Geophysics* 1994; **142**:419–445.
4. Das S. A numerical method for determination of source time functions for general three-dimensional rupture propagation. *Geophysical Journal of the Royal Astronomical Society* 1980; **62**:591–604.
5. Kame N, Yamashita T. Simulation of the spontaneous growth of a dynamic crack without constraints on the crack tip path. *Geophysical Journal International* 1999; **139**:345–358.
6. Lapusta N, Rice JR. Nucleation and early seismic propagation of small and large events in a crustal earthquake model. *Journal of Geophysical Research* 2003; **108**:2205. DOI: 10.1029/2001JB000793.
7. Andrews DJ. Rupture propagation with finite stress in antiplane strain. *Journal of Geophysical Research* 1976; **81**:3575–3582.
8. Andrews DJ. Test of two methods for faulting in finite-difference calculations. *Bulletin of the Seismological Society of America* 1999; **89**:931–937.
9. Andrews DJ. Rupture dynamics with energy loss outside the slip zone. *Journal of Geophysical Research* 2005; **110**:B01307. DOI: 10.1029/2004JB003191.
10. Day SM. Three-dimensional finite difference simulation of fault dynamics: rectangular faults with fixed rupture velocity. *Bulletin of the Seismological Society of America* 1982; **72**:705–727.
11. Madariaga R, Olsen KB, Archuleta RJ. Modeling dynamic rupture in a 3-D earthquake fault model. *Bulletin of the Seismological Society of America* 1998; **88**:1182–1197.
12. Duan B, Day SM. Inelastic strain distribution and seismic radiation from rupture of a fault kink. *Journal of Geophysical Research* 2008; **113**:B12311. DOI: 10.1029/2008JB005847.
13. Duan B. Effects of low-velocity fault zones on dynamic ruptures with nonelastic off-fault response. *Geophysical Research Letters* 2008; **35**:L04307. DOI: 10.1029/2008GL033171.

14. Ma S, Liu P. Modelling of the perfectly matched layer absorbing boundaries and intrinsic attenuation in explicit finite-element methods. *Bulletin of the Seismological Society of America* 2006; **96**:1779–1794.
15. Ma S, Beroza GC. Rupture dynamics on a bimaterial interface for dipping faults. *Bulletin of the Seismological Society of America* 2008; **98**:1642–1658.
16. Templeton EL, Rice JR. Off-fault plasticity and earthquake rupture dynamics: 1. Dry materials or neglect of fluid pressure changes. *Journal of Geophysical Research* 2008; **113**:B09306. DOI: 10.1029/2007JB005529.
17. Xing HL, Makinouchi A. Finite element modelling of frictional instability between deformable rocks. *International Journal for Numerical and Analytical Methods in Geomechanics* 2003; **27**:1005–1025.
18. Armero F, Garikipati K. Recent advances in the analysis and numerical simulation of strain localization in inelastic solids. In *Proceedings of Computational Plasticity IV*, Owen DRJ, Oñate E, Hinton E (eds). CIMNE: Barcelona, Spain, 1995; 547–561.
19. Borja RI, Regueiro RA. Strain localization of frictional materials exhibiting displacement jumps. *Computer Methods in Applied Mechanics and Engineering* 2001; **190**:2555–2580.
20. Borja RI. A finite element model for strain localization analysis of strongly discontinuous fields based on standard Galerkin approximation. *Computer Methods in Applied Mechanics and Engineering* 2000; **190**:1529–1549.
21. Chen Q, Andrade JE, Samaniego E. AES for multiscale localization modeling in granular media. *Computer Methods in Applied Mechanics and Engineering* 2011; **200**:2473–2482.
22. Larsson R, Runesson K, Sture S. Embedded localization band in undrained soil based on regularized strong discontinuity theory and FE analysis. *International Journal of Solids and Structures* 1996; **33**:3081–3101.
23. Linder C, Raina A. A strong discontinuity approach on multiple levels to model solids at failure. *Computer Methods in Applied Mechanics and Engineering* 2013; **253**:558–583.
24. Linder C, Rosato D, Miehe C. New finite elements with embedded strong discontinuities for the modeling of failure in electromechanical coupled solids. *Computer Methods in Applied Mechanics and Engineering* 2011; **200**:141–161.
25. Linder C, Armero F. Finite elements with embedded strong discontinuities for the modeling of failure in solids. *International Journal for Numerical Methods in Engineering* 2007; **72**:1391–1433.
26. Oliver J, Huespe AE. Theoretical and computational issues in modeling material failure in strong discontinuity scenarios. *Computer Methods in Applied Mechanics and Engineering* 2004; **193**:2987–3014.
27. Regueiro RA, Borja RI. Plane strain finite element analysis of pressure-sensitive plasticity with strong discontinuity. *International Journal of Solids and Structures* 2001; **38**:3647–3672.
28. Simo JC, Oliver J, Armero F. An analysis of strong discontinuities induced by strain-softening in rate-independent inelastic solids. *Computational Mechanics* 1993; **12**:277–296.
29. Simo JC, Rifai MS. A class of mixed assumed strain methods and the method of incompatible modes. *International Journal of Numerical Methods in Engineering* 1990; **29**:1595–1638.
30. Borja RI. Assumed enhanced strain and the extended finite element methods: a unification of concepts. *Computer Methods in Applied Mechanics and Engineering* 2008; **197**:2789–2803.
31. Dolbow J, Möes N, Belytschko T. An extended finite element method for modeling crack growth with frictional contact. *Computer Methods in Applied Mechanics and Engineering* 2001; **190**:6825–6846.
32. Ji H, Dolbow JE. On strategies for enforcing interfacial constraints and evaluating jump conditions with the extended finite element method. *International Journal for Numerical Methods in Engineering* 2004; **61**:2508–2535.
33. Liu F, Borja RI. Stabilized low-order finite elements for frictional contact with the extended finite element method. *Computer Methods in Applied Mechanics and Engineering* 2010; **199**:2456–2471.
34. Liu F, Borja RI. Finite deformation formulation for embedded frictional crack with the extended finite element method. *International Journal for Numerical Methods in Engineering* 2010; **82**:773–804.
35. Liu F, Borja RI. A contact algorithm for frictional crack propagation with the extended finite element method. *International Journal for Numerical Methods in Engineering* 2008; **76**:1489–1512.
36. Moës N, Dolbow J, Belytschko T. A finite element method for crack growth without remeshing. *International Journal for Numerical Methods in Engineering* 1999; **46**:131–150.
37. Sukumar N, Prevost JH. Modeling quasi-static crack growth with the extended finite element method part I: computer implementation. *International Journal of Solids and Structures* 2003; **40**:7513–7537.
38. Sukumar N, Moës N, Moran B, Belytschko T. Extended finite element method for three-dimensional crack modelling. *International Journal for Numerical Methods in Engineering* 2000; **48**:1549–1570.
39. Borja RI, Foster CD. Continuum mathematical modeling of slip weakening in geological systems. *Journal of Geophysical Research* 2007; **112**:B04301. DOI: 10.1029/2005JB004056.
40. Foster CD, Borja RI, Regueiro RA. Embedded strong discontinuity finite elements for fractured geomaterials with variable friction. *International Journal for Numerical Methods in Engineering* 2007; **72**:549–581.
41. Liu F, Borja RI. An extended finite element framework for slow-rate frictional faulting with bulk plasticity and variable friction. *International Journal for Numerical and Analytical Methods in Geomechanics* 2009; **33**:1535–1560.
42. Sanborn SE, Prevost JH. Frictional slip plane growth by localization detection and the extended finite element method (XFEM). *International Journal for Numerical and Analytical Methods in Geomechanics* 2011; **35**:1278–1298.
43. Svahn PO, Ekevid T, Runesson K. Discrete crack modelling in a new X-FEM format with emphasis on dynamic response. *International Journal for Numerical and Analytical Methods in Geomechanics* 2007; **31**:261–283.
44. Liu F, Borja RI. Dynamic fault rupture and propagation through a fixed finite element grid. In *Multiscale and Multiphysics Processes in Geomechanics*, Borja RI (ed.). Springer-Verlag: Berlin Heidelberg, 2011; 161–164.

45. Coon ET, Shaw BE, Spiegelman M. A Nitsche-extended finite element method for earthquake rupture on complex fault systems. *Computer Methods in Applied Mechanics and Engineering* 2011; **200**:2859–2870.
46. Fu P, Johnson SM, Carrigan CR. An explicitly coupled hydro-geomechanical model for simulating hydraulic fracturing in arbitrary discrete fracture networks. *International Journal for Numerical and Analytical Methods in Geomechanics* 2012. DOI: 10.1002/nag.2135.
47. Hunsweck MJ, Shen Y, Lew AJ. A finite element approach to the simulation of hydraulic fractures with lag. *International Journal for Numerical and Analytical Methods in Geomechanics* 2012. DOI: 10.1002/nag.1131.
48. Tu C-H, Chen C-S, Yu T-T. Fracture mechanics analysis of multiple cracks in anisotropic media. *International Journal for Numerical and Analytical Methods in Geomechanics* 2012; **35**:1226–1242.
49. Zhang Z, Gao H. Simulating fracture propagation in rock and concrete by an augmented virtual internal bond method. *International Journal for Numerical and Analytical Methods in Geomechanics* 2012; **36**:459–482.
50. Hughes TJR. *The Finite Element Method*. Prentice-Hall, Inc.: Englewood Cliffs, New Jersey, 1987.
51. Elguedj T, Gravouil A, Maigre H. An explicit dynamics extended finite element method. Part 1: mass lumping for arbitrary enrichment functions. *Computer Methods in Applied Mechanics and Engineering* 2009; **198**:2297–2317.
52. Gravouil A, Elguedj T, Maigre H. An explicit dynamics extended finite element method. Part 2: element-by-element stable-explicit/explicit dynamic scheme. *Computer Methods in Applied Mechanics and Engineering* 2009; **198**:2318–2328.
53. Menouillard T, Rethore J, Combescure A, Bung H. Efficient explicit time stepping for the extended finite element method (X-FEM). *International Journal for Numerical Methods in Engineering* 2006; **68**:911–939.
54. Collino R, Tsogka C. Application of the PML absorbing layer model to the linear elastodynamic problem in anisotropic heterogeneous media. *Geophysics* 2001; **66**:294–307.
55. Bielak J, Christiano P. On the effective seismic input for non-linear soil-structure interaction systems. *Earthquake Engineering and Structural Dynamics* 1984; **12**:107–119.
56. Belytschko T, Liu WK, Moran B. *Nonlinear Finite Elements for Continua and Structures*. John Wiley and Sons: New York, 2000.
57. Barenblatt GI. The mathematical theory of equilibrium cracks in brittle fracture. *Advances in Applied Mechanics* 1962; **7**:55–129.
58. Dugdale DS. Yielding of steel sheets containing slits. *Journal of the Mechanics and Physics of Solids* 1960; **8**:100–104.
59. Bilby BA, Cottrell AH, Swindon KH. The spread of plastic yield from a notch. *Proceedings of the Royal Society of London, Series A* 1963; **272**:304–314.
60. Ida Y. Cohesive force across the tip of a longitudinal shear crack and Griffiths specific surface energy. *Journal of Geophysical Research* 1972; **77**:3796–3805.
61. Palmer AC, Rice JR. The growth of slip surfaces in the progressive failure of overconsolidated clay. *Proceedings of the Royal Society of London, Series A* 1973; **332**:527–548.
62. Okubo PG, Dieterich JH. Effects of physical fault properties on frictional instabilities produced on simulated faults. *Journal of Geophysical Research* 1984; **89**:5817–5827.
63. Rummel F, Alheid HJ, Frohn C. Dilatancy and fracture-induced velocity changes in rock and their relation to frictional sliding. *Pure and Applied Geophysics* 1978; **116**:743–764.
64. Wong T-F. Shear fracture energy of westerly granite from post-failure behavior. *Journal of Geophysical Research* 1982; **87**:990–1000.
65. Dieterich JH. Modeling of rock friction: 1. experimental results and constitutive equations. *Journal of Geophysical Research* 1979; **84**:2161–2168.
66. Ruina AL. Slip instability and state variable friction laws. *Journal of Geophysical Research* 1983; **88**:10,359–10,370.
67. Borja RI, Sama KM, Sanz PF. On the numerical integration of three-invariant elastoplastic constitutive models. *Computer Methods in Applied Mechanics and Engineering* 2003; **192**:1227–1258.
68. Borja RI, Chao H-Y, Montáns FJ, Lin C-H. Nonlinear ground response at Lotung LSST site. *Journal of Geotechnical and Geoenvironmental Engineering* 1999; **125**:187–197.
69. Borja RI, Amies AP. Multiaxial cyclic plasticity model for clays. *Journal of Geotechnical Engineering* 1994; **120**:1051–1070.
70. Lamb H. On the propagation of tremors over the surface of an elastic solid. *Philosophical Transactions of the Royal Society of London* 1904; **203**:1–42.
71. De Hoop AT. A modification of Cagniard's method for solving seismic pulse problems. *Applied Scientific Research (B)* 1960; **8**:349–356.
72. Harris RA, Barall M, Archuleta R, Dunham E, Aagaard B, Ampuero JP, Bhat H, Cruz-Atienza V, Dalguer L, Dawson P, Day S, Duan B, Ely G, Kaneko Y, Kase Y, Lapusta N, Liu Y, Ma S, Oglesby D, Olsen K, Pitarka A, Song S, Templeton E. The SCEC/USGS dynamic earthquake rupture code verification exercise. *Seismological Research Letters* 2009; **80**:119–126.
73. Pollard DD, Fletcher RC. *Fundamentals of Structural Geology*. Cambridge University Press: U.K., 2005.